Journal Pre-proof

Achieving Single Solid Solution in Equimolar AlCrCuFeNi via Rapid Solidification

Ahmed Nassar, Hussain Al-Sairfi, Robert Cochrane, Mehmet Remzi Abul, Liam Teggin, Osama Al-Jenabi, Enrique Myro, Andrew Mullis

PII: S2352-4928(26)00281-3

DOI: https://doi.org/10.1016/j.mtcomm.2026.114897

Reference: MTCOMM114897

To appear in: *Materials Today Communications*

Received date: 21 July 2025
Revised date: 8 February 2026
Accepted date: 19 February 2026

Please cite this article as: Ahmed Nassar, Hussain Al-Sairfi, Robert Cochrane, Mehmet Remzi Abul, Liam Teggin, Osama Al-Jenabi, Enrique Myro and Andrew Mullis, Achieving Single Solid Solution in Equimolar AlCrCuFeNi via Rapid Solidification, *Materials Today Communications,* (2026) doi:https://doi.org/10.1016/j.mtcomm.2026.114897

Achieving Single Solid Solution in Equimolar AlCrCuFeNi via Rapid Solidification

Ahmed Nassar[a], Hussain Al-Sairfi[b,d], Robert Cochrane[b], Mehmet Remzi Abul[c], Liam Teggin[b], Osama Al-Jenabi[b], Enrique Myro[a], Andrew Mullis[b]

[a] *Brunel University London, BCAST, Uxbridge, United Kingdom*
[b] *School of Chemical and Process Engineering, University of Leeds, Leeds, LS2 9JT, UK*
[c] *School of Engineering, Ankara Yildirim Beyazit University, Kecioren, Ankara, Turkey*
[d] *Kuwaiti Institute for Scientific Research, P.O. Box: 24885, 13109 Safat, Kuwait*

Abstract

This study investigates the effect of cooling rate on the equimolar AlCrCuFeNi High-Entropy Alloy (HEA) using a 6.5m-tall drop-tube facility. It is found that as-cast AlCrCuFeNi comprises an FCC phase and a B2 phase. However, the AlCrCuFeNi alloy is found to attain a single B2 structure at cooling rates of 10^2 K/s and above. The cooling rates achieved in this work are estimated to vary between 112 K/s and 1.13×10^6 K/s. Phase separation within the dendrites is observed in the as-cast alloy. This phase separation occurs via spinodal decomposition and is inhibited only at the highest achieved cooling rate of around 1.13×10^6 K/s. As such, with higher cooling rates, simpler microstructures are obtained, extending the solid-solution of the system. This is one of the primary objectives in employing rapid-solidification techniques in HEAs. Finally, the microhardness of the rapidly cooled samples is probed and found to increase with cooling rate. Notable jumps in microhardness are noted and related to changes in morphology.

Graphical Abstract

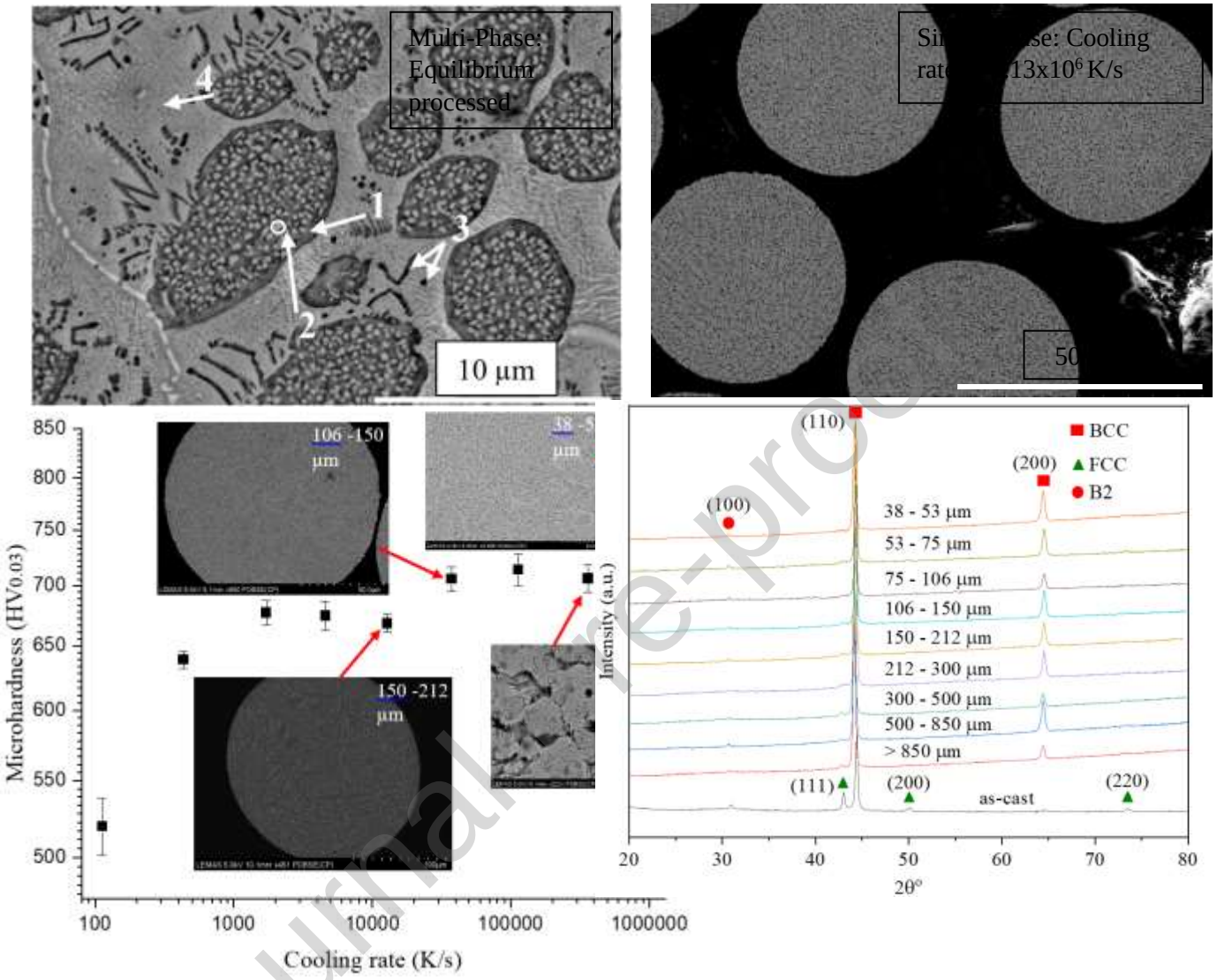

Keywords: High-Entropy Alloy; Spinodal decomposition; Solidification microstructure; Hall-Petch; Rapid-solidification.

1. Introduction

For the past two decades High-entropy alloys (HEAs) have shown promise in a wide range of applications and continue to attract great academic attention. The definition of HEAs has been updated frequently, with today's general consensus being that an HEA comprises at least five elements with no element contributing less than 5 % of atomic percentage [1]. HEAs that exhibit single-phase solid solutions attracted most attention in the early days [2,3], although multi-phase HEAs have been attracting increasing attention in recent years [4–6]. In general, HEA lattices are simple-solid solutions such as FCC, BCC or HCP [7,8]. Due to the presence of multiple elements, a large entropy of mixing ΔS_{mix} reduces the Gibb's free energy of these solutions, making them stable [9,10]. However, a central issue with HEAs that persists until today

lies in achieving a strength-ductility balance in the alloys [11]. HEAs with FCC crystal lattices typically have good ductility but relatively low strength, whereas BCC-type HEAs typically have high strength and compromised ductility [12]. As such, achieving duplex (FCC + BCC) HEAs is beneficial in resolving this strength vs ductility trade-off.

In the present study, we investigate the duplex AlCrCuFeNi alloy and the effect of cooling rate on its morphology and microhardness. Arc-melted, equimolar AlCrCuFeNi has previously been shown to comprise FCC and BCC phases [13], together with a compound phase which Jingon *et al.* have reported as $Al(Fe_{0.23}Ni_{0.77})$ with a volume fraction reported to be 18% (obtained via XRD peak intensity analysis) [14]. Other studies have identified the compound phase as AlNi [13,15]. It is therefore most likely that this B2-ordered intermetallic is $AlNi_xFe_{1-x}$, where Fe randomly substitutes Ni at different levels. It is clear from the mechanical studies on AlCrCuFeNi that despite the presence of a compound phase, it is a HEA with interesting mechanical properties as it has shown a plastic strain of around 15 % [16] and fracture strength of 1750 MPa [13]. AlCrCuFeNi has also been manufactured via other techniques such as Vacuum Levitation (VL) and Selective Laser Melting (SLM). The VL method appears to have inhibited the formation of the compound phase [17], whereas the rapid cooling rate of SLM inhibits the formation of the FCC phase completely, resulting in a single B2 solution [13]. Due to the loss of the FCC phase in SLM-ed AlCrCuFeNi, the alloy is reported to have high crack sensitivity.

Although there are studies which explore the AlCrCuFeNi system using different manufacturing techniques and heat treatments [18], there is no single study which investigates a wide variety of cooling rates on this alloy. As such, our work is the first to report a wide range of powder sizes, a large variety of cooling rates and, in turn, microstructures of the AlCrCuFeNi HEA. Of the few studies which dedicate significant attention to the AlCrCuFeNi system, attention is mainly given to the effect of elemental variations on the HEA's properties [19] and there is no detailed focus on microstructural development or cooling rate variation. Investigating the potential strengthening effect due to grain refinement of the AlCrCuFeNi system is important in discovering a Co-free, economic, and high-performance HEA.

In general, the effect of rapid solidification on HEAs is a relatively under-explored topic despite its potential of unveiling novel materials [20]. As such, the drop-tube technique used in this work is applied with the motivation of attaining rapidly cooled droplets with simpler structures than their respective master alloys. Furthermore, the high cooling rates may lead to disorder trapping of the ordered phases, also leading to simpler structures in the drop-tube-processed droplets.

In this study, the AlCrCuFeNi alloy master alloy is fabricated using arc-melting and processed using a drop-tube facility to attain rapidly cooled droplets of varying sizes, such that the diameters of each size-fraction are: $d > 850$, $500 < d < 850$, $300 < d < 500$, $212 < d < 300$, $150 < d < 212$, $106 < d < 150$, $75 < d < 106$, $53 < d < 75$ and $d > 38$, where d is droplet diameter measured in μm. The microstructures of the master-alloy and its rapidly-cooled droplets are studied using SEM and EDX techniques. XRD analysis is used to identify the phases present in the samples and TEM is carried out on the slowest cooled sample (112 K/s) to develop an understanding for the complexity of its structure and its decomposition processes.

2. Methodology

2.1 Alloy fabrication

An ingot of the alloy was prepared using an arc-melter operated at a current of 230 A with a water-cooled copper hearth. The arc-melter's vacuum chamber (0.05 mbar) was purged with Argon gas four times before each melt. To ensure homogeneity, the alloy was turned over and melted five times. The constituent elements of the manufactured alloy had a purity of > 99.9 wt%.

2.2 Drop tube experiment and cooling rate estimation

A drop tube of 6.5m in length was pre-evacuated to pressures below 10^{-4} Pa before being back-filled with 50 kPa of pure N_2 gas. A schematic of the apparatus is shown in Fig. 1.

A 7.3g as-cast ingot was placed in an alumina crucible containing three holes at its base, and inductively heated using a 3 kW RF power supply until its melting point was attained. The liquid metal was then ejected from the crucible using a differential pressure of 350 kPa. The majority of droplets solidified containerlessly in-flight, allowing for high undercooling [21], and were collected at the bottom of the drop-tube. The resulting powders were manually sieved into the aforementioned diameter ranges.

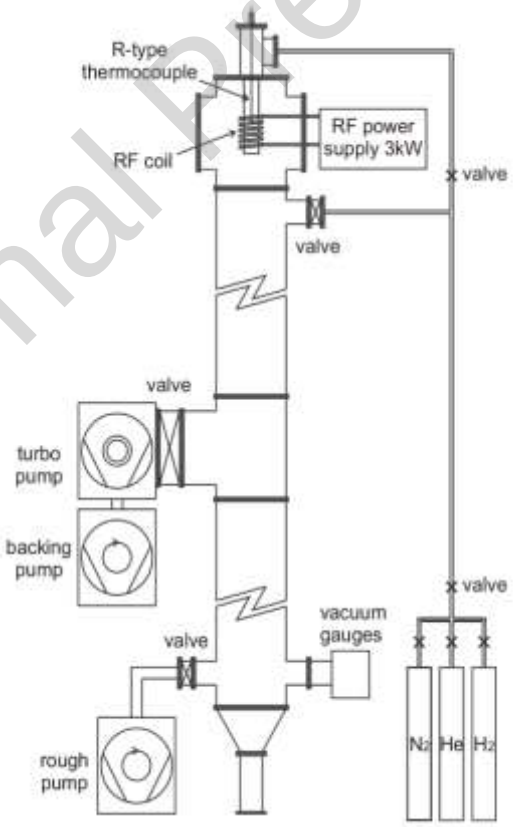

Fig. 1. Schematic of Drop-Tube apparatus used in this work.

To calculate the cooling rate of each powder size fraction, a heat balance for a droplet in free fall was used which considers heat transfer via convection, conduction and radiation from the droplet to its environment. This heat balance is expressed as shown in Equation 1 [22]. As a result of the drop tube experiment, a range of cooling rates is achieved and in turn, a range of powder sizes and microstructures. Although there is an expected difference in the cooling rate between the outside of each particle and its center, the heat balance analysis conducted in this work cannot give such a cooling rate profile.

$$\frac{dT_d}{dt}[c_l(1-f)+c_s f]+L\frac{df}{dt} = \frac{6h}{\rho d}\left(T_d - T_g\right)+\frac{6\varepsilon\sigma_b}{\rho d}\left(T_d^4 - T_g^4\right) \quad (1)$$

where T_g is the temperature of the gas used to back-fill the apparatus (N_2), c_s and c_l are the specific heat of the metal in the solid and liquid states, respectively, f is the solid fraction, ρ is the density of the solid metal, d the diameter of the droplet, ε the emissivity of the droplet surface, σ_b the Stefan–Boltzman constant, T_d is the instantaneous temperature of the particle, L is the latent heat of fusion, and h is the heat transfer coefficient, which is evaluated according to the assumption that the particles attain terminal velocity within the tube during free fall.

The heat transfer coefficient, h, is given by:

$$h = \frac{\kappa_g}{d}(2.0 + 0.6\sqrt{Re}\,3\sqrt{Pr}) \quad (2)$$

where κ_g is the thermal conductivity of the Nitrogen gas, Re is the Reynolds number and Pr is the Prandtl number. The Reynolds and Prandtl numbers are given by the following equations:

$$Re = \frac{\nu_g \rho_g D}{\eta_g} \quad (3)$$

$$Pr = \frac{c_g^p \eta_g}{\kappa_g} \quad (4)$$

Where ν_g, ρ_g, η_g and c_g^p are the flow velocity, density and dynamic viscosity and specific heat of the back-fill gas, respectively.

2.3 Sample analysis

The ingots obtained from the arc-melter and the drop-tube atomized powders were hot mounted using Transoptic resin and grounded using abrasive SiC paper from the P800 down to the P2500 size. The mounted alloys were then polished manually using 6 µm, 3 µm and 1 µm diamond paste, followed by automatic polishing using Colloidal Silica. The samples were then etched with aqua regia solution for 10 - 15 seconds to be observed under a Hitachi SU8230 scanning electron microscope (SEM). The SEM was used in backscattered electron detection mode to examine the microstructures of the samples. EDX analysis was used to analyse the compositions of the phases observed in the microstructures and to ensure homogeneity.

XRD (Bruker D8) was used to obtain the patterns in this work, using Cu-Kα radiation with a scanning rate of 1º/min and a range from 20º to 80º. Microhardness measurements were performed (using Tukon 1202 Wilson) on all powder sizes using a load of 300 gf with a dwell time of 10 seconds. Ten measurements were taken for each powder size fraction to minimise standard error. Rietveld refinement was not performed due to the lack of established structure factors and unknown atomic site occupancies in the B2 lattice. Further, the high cooling rates likely induce 'disorder trapping,' meaning refinement would quantify the degree of ordering rather than the true physical phase fraction. As such, raw pointwise diffraction data were analysed without post-processing smoothing.

TEM analysis was carried out using the FEI Titan Themis Cubed operated at 300kV and fitted with a monochromator and Super-X EDX system with windowless 4-detector design. Bright-field TEM images were collected using the Gatan OneView 16 Megapixel CMOS digital camera. A probe current of 200pA was used to collect EDX spectra with a dwell time of 20 μs and HAADF camera length of 115mm. GMS3 and Velox software was used to collect and process the data.

ImageJ software is used to measure the area of the dendrites. Due to the fragmented nature of the dendrites in the microstructures produced in this work, grain refinement is measured as a function of the dendrite area rather than a more common measure such as secondary dendrite arm spacing.

Table 1

Properties of AlCrCuFeNi HEA [23,24]					
c_s J kg^{-1} K^{-1}	c_l J kg^{-1} K^{-1}	ρ kg m^{-3}	L kJ kg^{-1}	ε	T_m K
479	551	6770	296	0.2	1330
Properties of N_2 Gas [25]					
T_g K	η_g	ρ kg m^{-3}	c_g^p J kg-1 K	κ_g	-
295	1.78×10^{-5}	1.16	1039	2.60×10^{-2}	

2.4 Particle size analysis

The particle size distribution (PSD), shown in Fig. 2 was found to follow a log-normal distribution $\sigma_{LN} = 2.98$ with a mass median diameter d(m, 50) of 366µm and a mode of around 110µm. The relatively large value for σ_{LN} explains the broad range of particle sizes produced in a single experimental run. Although the mass is skewed toward larger fractions, a conversion to a number distribution yielded a significantly smaller median d(n, 50) of 10.2 µm. This confirms that all size fractions are numerically dominated by smaller particles, which is the primary factor driving the observed solidification microstructures and cooling rate estimates.

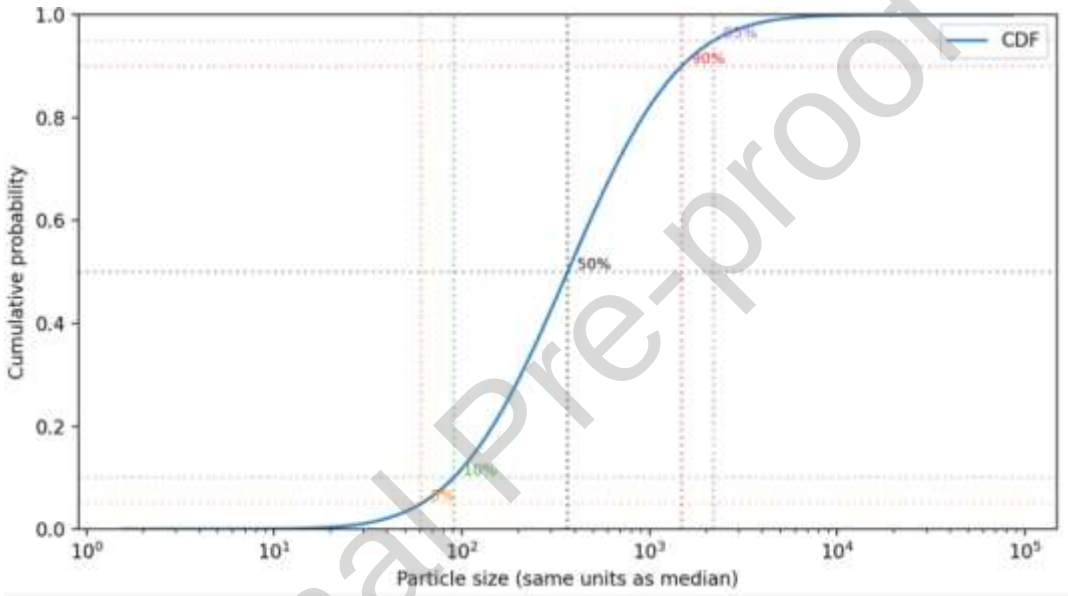

Fig. 2. Mass-based cumulative distribution function of AlCrCuFeNi powder. The data follows a log-normal distribution with a mass-median diameter of 366µm and geometric standard deviation of 2.98.

3. Results

3.1 XRD and microstructure analysis

Fig. 3 shows the XRD traces of as-cast AlCrCuFeNi and AlCrCuFeNi powders. It is evident that the FCC peaks observed in the as-cast alloy decrease in intensity until unobservable in the 38 – 53 μm size fraction. The XRD trace of the 38 – 53 µm droplets therefore suggests a single-phase B2 structure, whereas the traces from 500 – 850 µm down to the 53 – 75 µm size-fraction show that the FCC is not inhibited, though it is restricted.

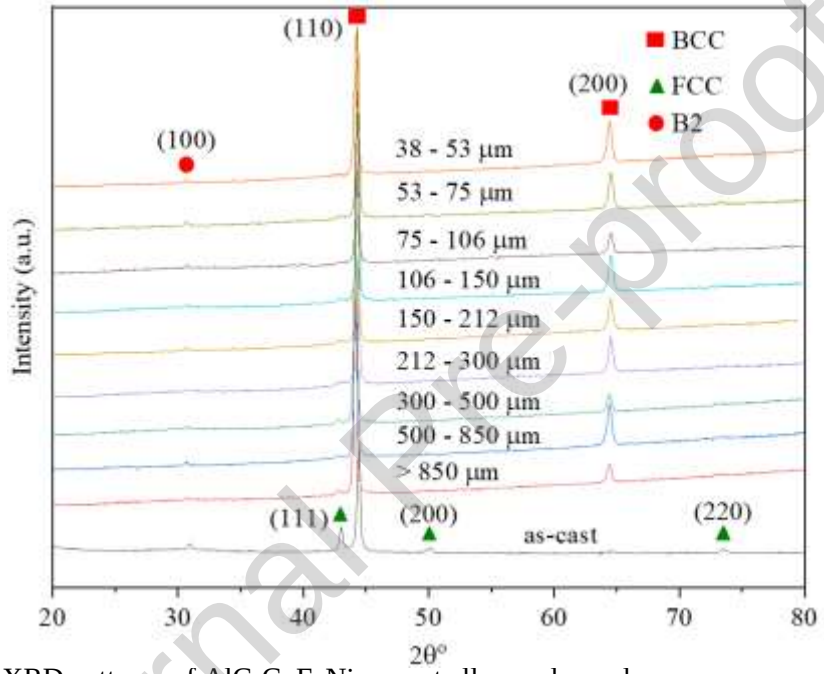

Fig. 3. XRD patterns of AlCrCuFeNi as-cast alloy and powders.

Fig. 4 shows a SEM backscattered electron image of the as-cast AlCrCuFeNi alloy. Its microstructure exhibits a dendritic structure that possesses four distinct phases: the dendritic region (D), precipitates within the dendrites, a needle-like intermetallic (IM) seen along the periphery of the dendrites and deeper within the ID region, and finally, the inter-dendritic (ID) matrix. These are labelled as 1-4 in Fig. 4 in their respective order. It is observed in Fig. 4 that the IM (labelled as 3) in the matrix appears in a spherical form as well as sharp needles of varying complexity. The precipitates (labelled as 2) appear to be evenly distributed within the dendrites and consistent in size, which appears to be of the nano-scale. An EDS analysis presented in Table 2 shows the Cu content in the ID regions of the as-cast alloy to be dominant and particularly higher than the content of Cr and Fe. Considering the relatively large, positive enthalpies of mixing between Cu and each of Cr and Fe (12 kJ mol^{-1} and 13 kJ mol^{-1} respectively) [26], Cu segregation is expected. This small bonding energy of Cu with Cr and Fe leads to separation in the ID region which, as seen from Table 2, leads to an atomic percentage of Cu in the ID region of near 50 %. Cu segregation, particularly in a plate-like manner, has previously been observed in several HEAs comprising similar principal elements, such as $Al_{0.5}CrCuFeNi_2$ [27] and $Al_2CoCrCuFeNi$ [28] AlCoCrCuFeNi [29]. Although Al and Ni contribute to the ID region, they also form a significant part of the dendritic region, where they are not expected to form a fully homoegnous structure with Cr and Fe due to the precipitates observed.

The microstructure of an AlCrCuFeNi droplet from the d > 850 μm size fraction (cooled at an estimated 112 K/s) is presented in Fig. 5, showing its strong similarity to the as-cast sample. It is therefore clear that this cooling rate is not sufficient to suppress the growth of the needle-like structure and that higher cooling rates are required to achieve a simple solid-solution or a simpler microstructure in general. Nevertheless, the microstructure does appear less complex as cooling rate increases. This is observed in Fig. 6 which shows the microstructures of powder cooled at 3.74×10^4 K/s, where at low magnification this sample (from the 106 – 150 μm size fraction) appears to comprise a simple solid-solution structure. At higher magnifications, however, it appears that the needle-like aggregates are still present, as observed in Fig. 6b and Fig. 6c. The precipitates within the dendrites are also retained at this cooling rate, with their scale being refined to the order of a few nanometers. In powders of this size fraction the dendrites are fragmented, as seen in the cases of the droplets of larger size fractions and the master alloy.

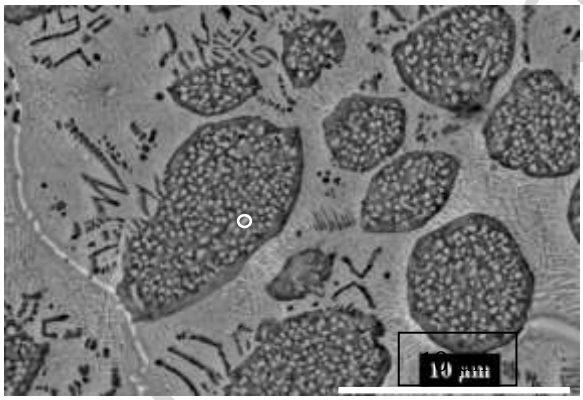

Fig. 4. Backscatter SEM images of as-cast equimolar AlCrCuFeNi microstructure.

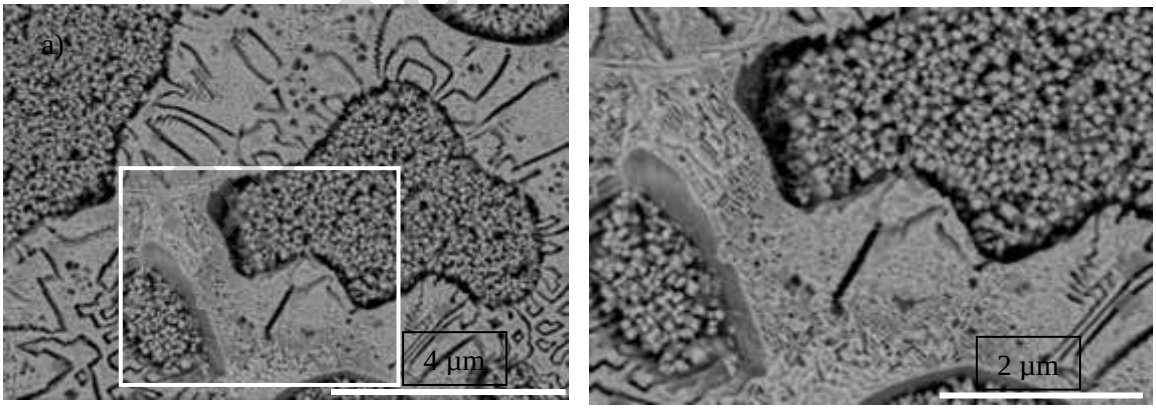

Fig. 5. Microstructure of AlCrCuFeNi d > 850 μm powder (cooled at an estimated 112 K/s).

At the highest cooling rate of around 1.13×10^6 K/s, a microstructure free of IM phases is observed in powders of the 38 – 53 μm size fraction (see Fig. 7). The microstructure in this powder range shows a much closer resemblance to a typical single-phase solid-solution. These powders show a simple dendritic structure where critical observations can be made that are the dendrites appear to be free of precipitates and the ID phase appears to be free of the needle-like structure observed at lower cooling rates. This observation is an important one as it demonstrates that expanding the boundary of HEAs via rapid cooling is possible.

A microstructure such as that seen in Fig. 7 is obtained due to the rapid cooling rates that achieve large enough undercoolings, which in turn trap metastable phases and possibly induce disorder trapping.

Table 2.
Elemental analysis of as-cast AlCrCuFeNi master alloy.

Region	Element (at%)				
	Al	Cr	Cu	Fe	Ni
D	12.53	31.00	8.89	30.07	17.51
ID	20.62	3.38	47.28	6.52	21.75

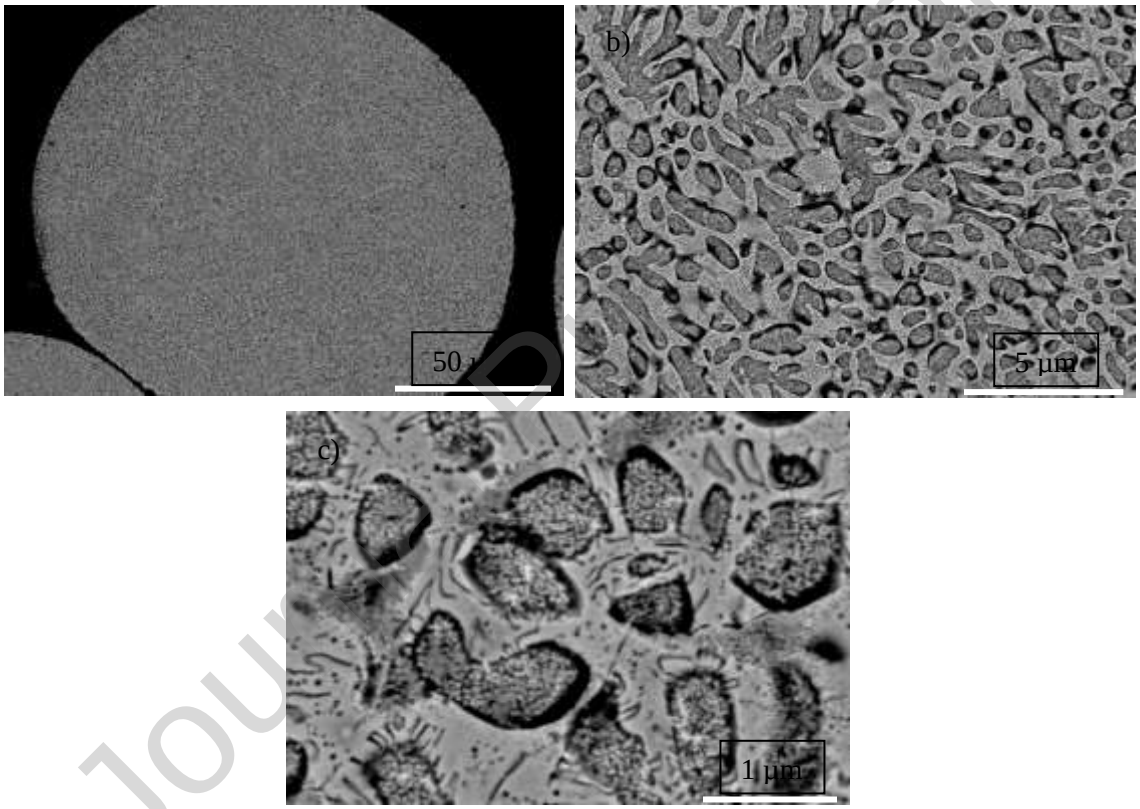

Fig. 6. Microstructure of 106 – 150 μm AlCrCuFeNi powder, cooled at estimated 3.74×10^4 K/s

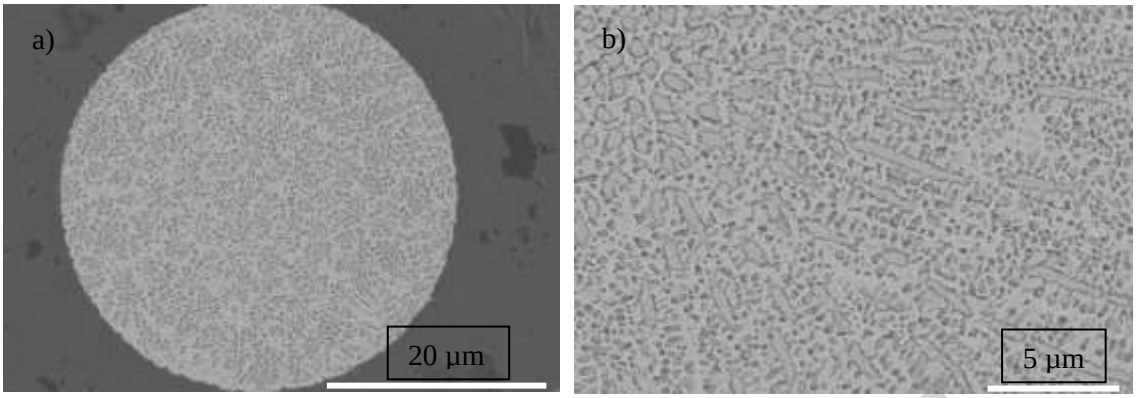

Fig. 7. Microstructure of 38 – 53 μm powder cooled at an estimated 1.13×10^6 K/s. **a)** Lower magnification shows a simple solid-solution and **b)** higher magnification confirms the disappearance of needle-like IM phase and precipitates within the dendrites.

3.2 TEM analysis

TEM analysis on the as-cast sample confirms the duplex nature of the master alloy and is in accord with our SEM and XRD results. A Bright-Field (BF) image of an inter-dendritic region in the as-cast sample is shown in Fig. 8a, where the ID matrix is labelled as '1' and the IM regions are labelled as '2'. The SAD patterns of these phases are presented in Fig. 8b and Fig. 8c, where it can be seen that the IM regions are B2 ordered and the ID matrix comprises an FCC structure. These phases have lattice parameters of 2.63 Å and 3.49 Å, respectively.

TEM analysis is also carried out on the d > 850 μm powders, wherein the IM needles are shown to be Cr-Fe rich and the ID region rich in Al-Ni-Cu. Unlike the as-cast sample, the ID region of the d > 850 μm droplet is found to comprise an ordered B2 structure (shown by the SAD pattern in Fig. 9a), indicating that the FCC of the ID region is inhibited at this cooling rate of 112 K/s. This is compatible with the XRD data in Fig. 3, which shows a significant drop in the intensity of the FCC peak in the d > 850 μm scan. Judging by the SAD pattern of Fig. 9b, the B2 ordered structure of the needle-like IM appears to be retained. Between the needle-like structures in Fig. 9, weak intensity bands of Cr and Fe are present which are only observed in TEM EDS mapping. Referred to in Fig. 9e and Fig. 9g as inter-needle bands, these may represent needle intermetallics which had not developed completely prior to solidification.

Fig. 10a shows a BF image of the dendritic region in the d > 850 μm sample. SAD patterns are taken from the precipitates within the dendrites and from the dendrite itself, showing that both phases comprise ordered B2 structures. These SAD patterns are shown in Fig. 10b and Fig. 10c. The lattice parameters of the dendrite and the precipitates (within the dendrites) are found to be 2.43 Å and 2.42 Å, respectively. HAADF imaging and elemental distribution maps of a dendritic region in the same sample are shown in Fig. 11, where it is evident that the precipitates are rich in Al and Ni and the dendrite mainly comprises Cr and Fe. This is a commonly observed separation of elements due to the favourable, negative enthalpies of mixing between Al-Ni and Cr-Fe. On the dendrite's periphery (in the ID region) plate-like Cu separation is observed which takes place in addition to the bulk segregation of Cu. In addition to these plate-like nano-precipitates, globular Cu precipitates are also observed in the ID region. These are shown in the elemental distribution maps of Fig. 12.

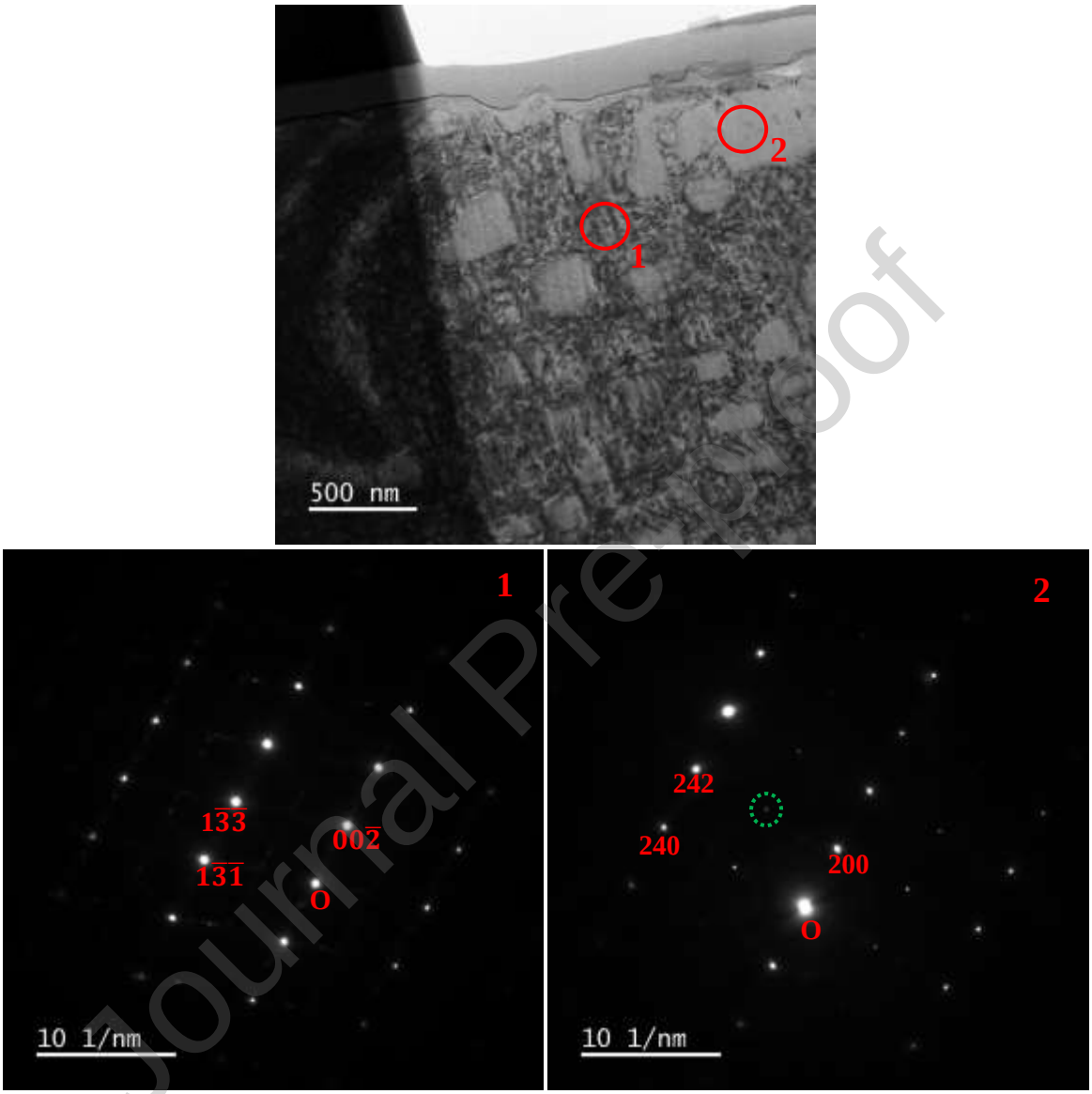

Fig. 8. a. ID region from the as-cast alloy, including IM phases**. b.** [3 1 0] SAED pattern from ID phase showing FCC structure**. c.** [2 1 0] SAED pattern from 'needle-like' phase showing B2 ordering, where the green circle highlights the superlattice spots.

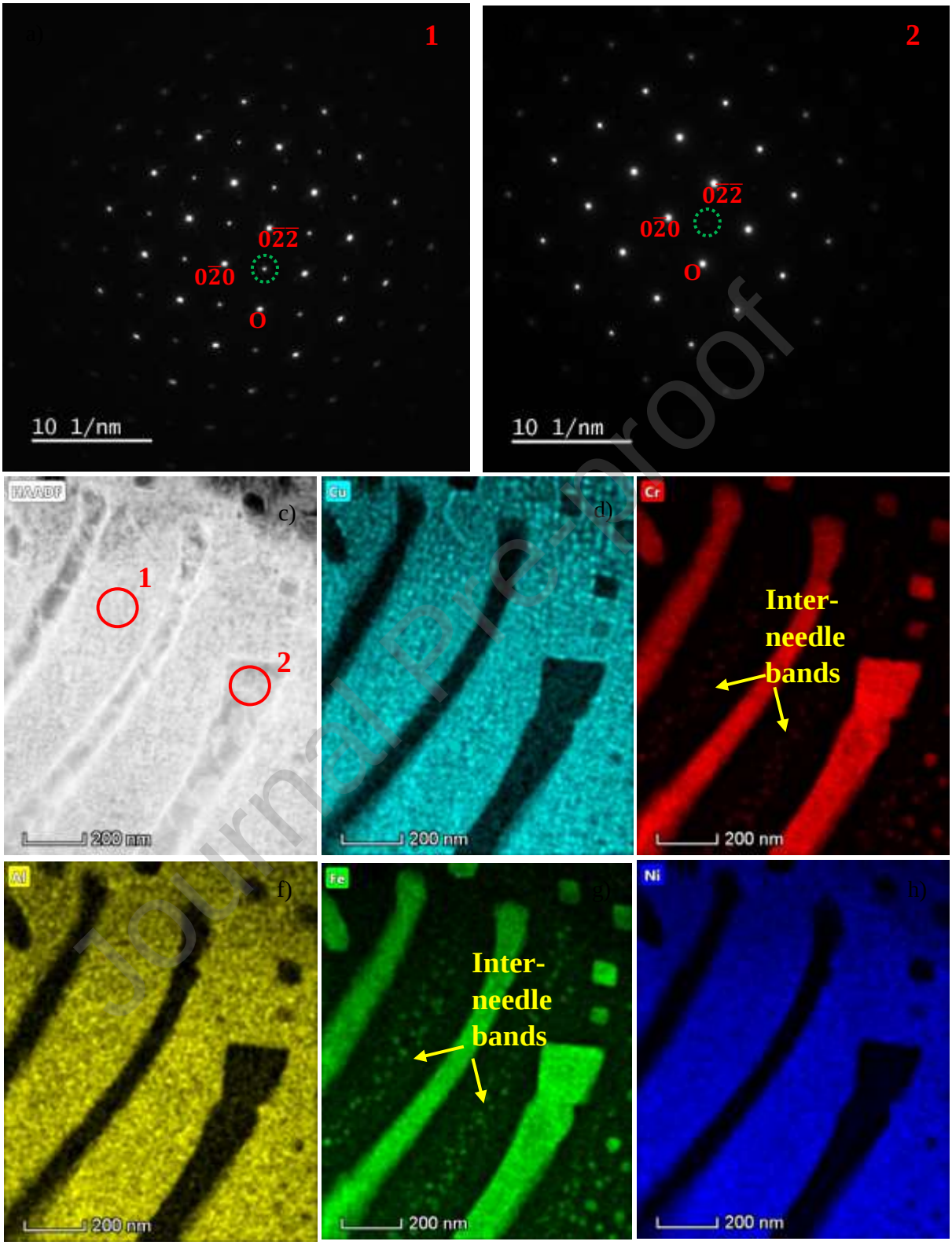

Fig. 9a: SAD pattern from ID region [1 0 0] zone axis, **b:** SAD pattern from IM [1 0 0] zone axis **c:** HAADF image **d-h:** elemental distribution from ID and IM regions in d > 850 μm sample.

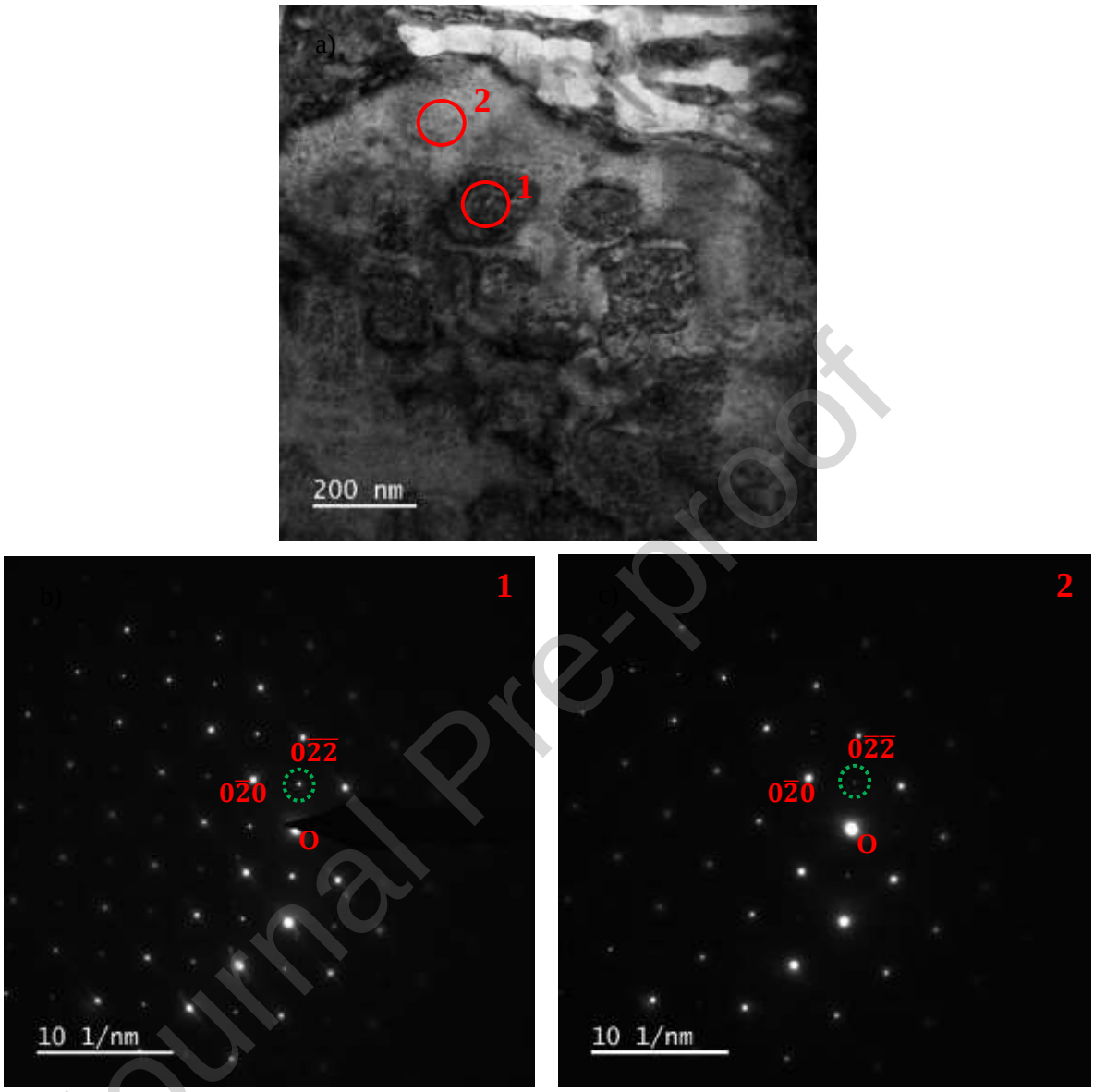

Fig. 10. a: Dendritic region from droplet of the d > 850 µm size-fraction **b:** [0 0 -1] SAD pattern of precipitates within the dendrite **c:** [0 0 -1] SAD pattern of precipitate-free region within the dendrite.

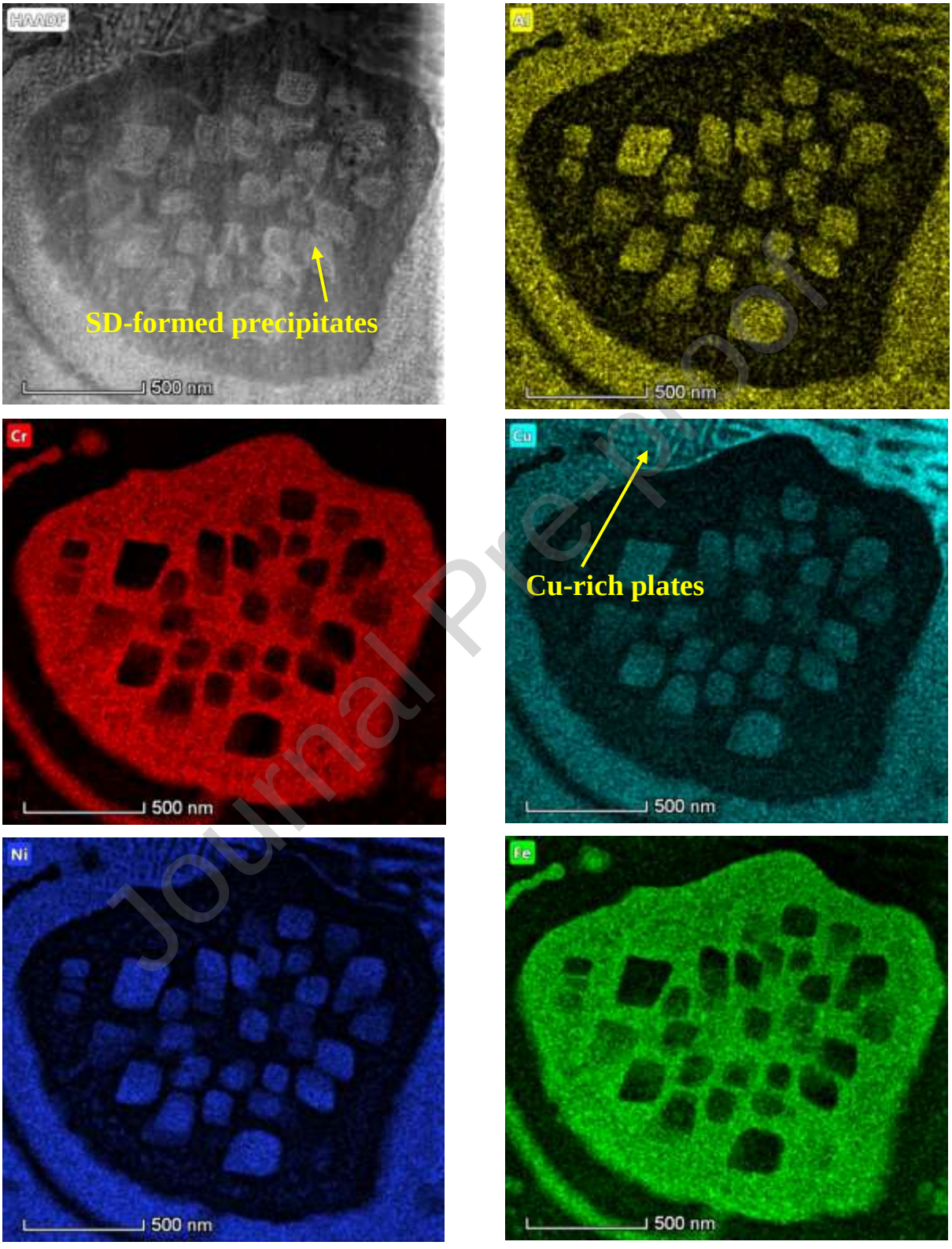

Fig. 11. HAADF image and elemental distribution images of dendritic region in AlCrCuFeNi sample cooled at 112 K/s.

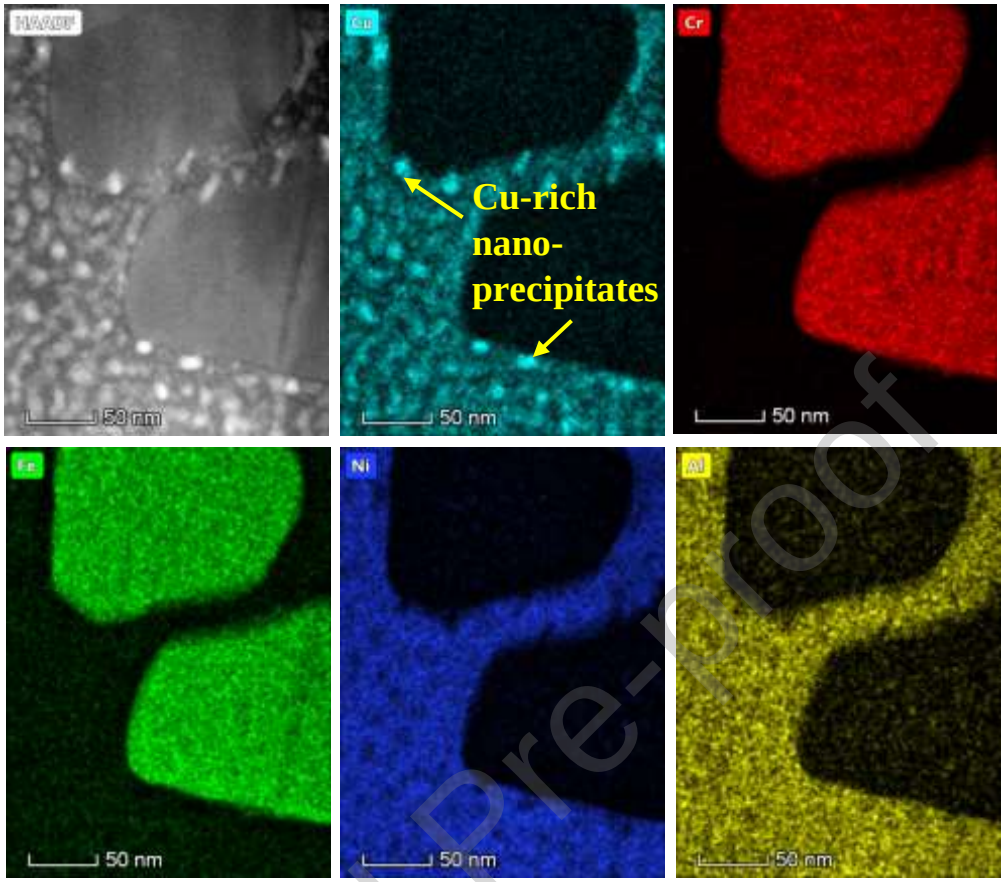

Fig. 12. HAADF image and elemental distribution images from ID region in sample cooled at an estimated 112 K/s.

3.3 Grain refinement and microhardness

Gradual refinement is observed with increased cooling rate, where the equivalent diameter of the dendrites, d_{eq}, decreases from a mean value of 3.86 μm in the d > 850 μm size fraction to 0.47 μm in the 53 – 75 μm size fraction. Although secondary dendritic arm-spacing is the most common measurement of grain refinement, in this work it is measured as a function of dendrite area due to the fragmented nature of the dendrites. Namely, the square root of the measured area is multiplied by a factor of $\frac{2}{\sqrt{\pi}}$, in order to obtain the equivalent diameter of the fragmented dendrite.

To understand the effect of rapid cooling on the microhardness of the AlCrCuFeNi HEA, Vickers microhardness measurements were made on the powders obtained from the alloy. In the Hall-Petch plot of Fig. 13, the alloy shows an overall increase in microhardness as the dendrites become finer. This confirms the positive effect of grain refinement on the microhardness of the powders. An outlier with low microhardness is observed at $A^{-0.25}$ = 0.74 (d > 850 μm size fraction), which is explained by the larger FCC residue than other samples (it being known that FCC is the softer phase). To aid in correlating the powders presented in this work to their respective cooling rates, Fig. 14 relates droplet size with cooling rate. Further, microhardness is plotted against cooling rate, in order to better correlate microstructure/particle size to microhardness. This plot is seen in Fig. 15, where the largest powder sieve

fraction (d > 850 μm) has a microhardness of 519 $HV_{0.03}$ and the smallest powder sieve fraction (38 – 53 μm) shows a microhardness of 805 $HV_{0.03}$, confirming the increase in microhardness due to grain refinement. While there is an overall increase, it appears as though there are certain developments in the morphology of the alloy to which the jumps in microhardness are attributed. The micrographs included in Fig. 15 attempt to explain the jumps in microhardness from the 150 – 212 μm to the 106 – 150 μm and from the 53 – 75 μm to the 38 – 53 μm size fractions.

Naturally, grain refinement is the principal factor in these witnessed increases in microhardness. However, these changes in microstructure are highlighted to allow correlating the alloy structure to its microhardness. It can be seen that from the 150 – 212 μm to the 106 –150 μm size fractions, the morphology changes from being evidently dendritic to a more fragmented appearance, where the dendrites are only observable at higher magnifications – Fig. 6 provides a closer look at this morphology. As for the increase seen between the (53 – 75 μm) to the (38 – 53 μm) size fractions, Fig. 7 shows that this is the critical point where the microstructure of the powders loses the needle-like structures in the matrix and achieves a simple solid solution. In the regions where microhardness does not vary with cooling rate, it is suspected that the decreasing concentration of nano-precipitates within the dendrites has a negative effect on hardness, cancelling out the effect of grain refinement.

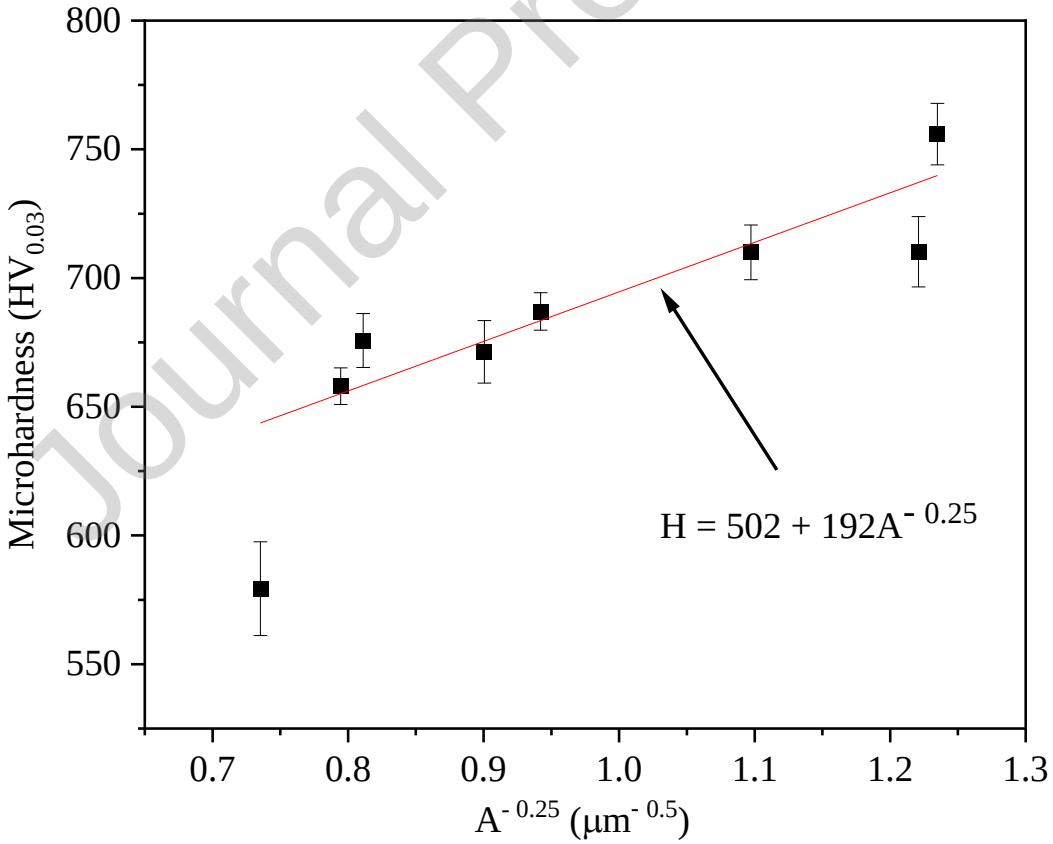

Fig. 13. Microhardness of AlCrCuFeNi powders as a function of $A^{-0.25}$ in a Hall-Petch plot.

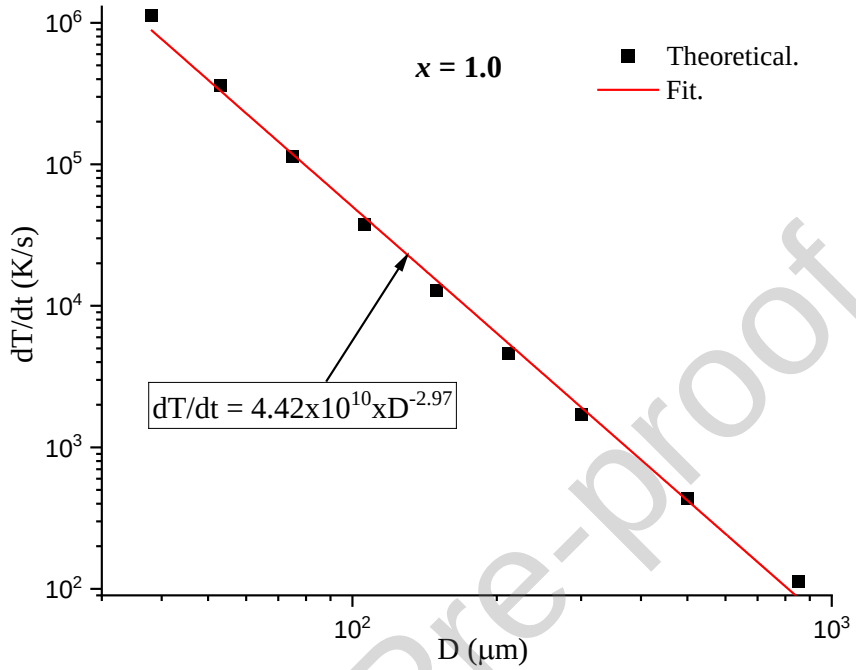

Fig. 14. Estimated cooling rate as a function of powder diameter.

4. Discussion

In this work, non-equilibrium cooling of equimolar AlCrCuFeNi HEA is achieved using a drop-tube facility such that cooling rates between 112 K/s and 1.13×10^6 K/s are attained. As-cast AlCrCuFeNi is also investigated and found to comprise FCC and B2 phases. A needle-like IM phase is observed in the ID region of the as-cast alloy and identified to be a B2 ordered phase, whereas the ID region is FCC ordered. The B2 ordered IM can be seen in Fig. 4 where it is labelled as phase '3'. Phase separation within the dendrites is also observed in the as-cast alloy. We conclude that the precipitates within the dendrites form via spinodal decomposition in the solid-state due to their nature in appearing consistently in the microstructure's dendrites and their even distribution within the dendrites. This argument is further supported by the fact that the precipitates and the dendrites comprise the same crystal structure (both B2 ordered). Spinodal decomposition has also been observed previously in alloys of a similar base, particularly in the AlCoCrCuFeNi system [30].

Our TEM analysis shows that the AlCrCuFeNi HEA attains a single B2 structure at cooling rates of 112 K/s and above. The SAD patterns in Fig. 9 and Fig. 10 form a full picture of the phases in the sample cooled at 112 K/s, where Fig. 9 shows the B2 ordering in the IM phase and the ID region, and Fig. 10 shows the B2 ordering of the dendrites and their precipitates. As such, it is evident that FCC growth is mostly inhibited at this cooling rate. This is relatively similar to an observation made by R. Wang et al., who show that FCC growth in the duplex (FCC/BCC) AlCoCrFeNi HEA is inhibited due to the cooling rate experienced during laser fabrication [31]. However, although their study does prove the inhibition of FCC growth, there is no mention of the cooling rate at which this occurs. Contrary to our work and the work of R. Wang et al. is the

observation made by Y. Wang et al., which claims that in the equimolar AlCoCrCuFeNi HEA, it is the growth of the BCC which is restrained due to selective laser melting (though not completely inhibited), rather than the FCC [32]. Despite the slight difference in constituent elements, it would be expected that the AlCoCrCuFeNi HEA would show the same general behavior as its Cu-free variant. Nevertheless, given that our as-cast is sample expected to have a cooling rate of around 10 – 20 K/s, it can be said that the FCC structure is lost between 20 K/s and around 112 K/s. The XRD traces in Fig. 3 are in accord with the observation that FCC growth is suppressed, as the intensity of the FCC peak is dramatically reduced and almost unobservable in the powders. The weak FCC peaks which remain are due to the stochastic nature of nucleation (and hence droplet undercooling), in that the FCC phase is likely being retained in some, but not all droplets. This accounts for the decreased intensity of the FCC peaks in the XRD spectrum (fewer droplets with FCC) and is also consistent with not seeing the FCC phase in the single TEM sample taken in Fig. 9.

Between the needle-like structures, weak intensity bands of Cr and Fe are present which are only observed in TEM EDS mapping. Referred to in Fig. 9e and Fig. 9g as inter-needle bands, these are likely to be 'embryonic' needles, in that the structure solidified prior to forming fully developed needles. It is expected that the SAD pattern from the area between the needles also shows a B2 structure, since both the ID matrix and the needle-like phase are B2 ordered. It is indeed observed in the SAD pattern (Fig. 9a) of the 'inter-needle region' that there appears to be a slight overlap in patterns between the B2 structure of the ID region with that of the Cr and Fe rich bands. Given that the inter-needle spacing is around 400 nm, it is likely that these have formed via solid-state diffusion rather than growth from the liquid.

At the highest cooling rate of around 1.13×10^6 K/s, a microstructure free of IM phases is observed in powders of the 38 – 53 μm size fraction. A microstructure from this size fraction is displayed in Fig. 7 and shows a much closer resemblance to a typical single-phase solid-solution. Just as the ID phase appears to be free of the needle/ribbon-like IM observed at lower cooling rates, the dendrites also appear to be free of precipitates. Due to one of the core characteristics of HEAs that is sluggish diffusion, it would be expected that the solid-state spinodal decomposition which gives rise to these precipitates would be suppressed at cooling rates of lower magnitude. Nevertheless, Fig. 7 shows that with higher cooling rates, simpler microstructures can be obtained and the extension of the solid-solution of HEAs is possible via drop tube rapid-solidification technique.

Grain refinement is observed in the powders and is measured as a function of equivalent diameter (d_{eq}). The fragmented nature of the dendrites makes it impossible to use a more common measure of grain refinement such as secondary arm spacing. Nevertheless, the measurement of d_{eq} gives a clear idea about the grain refinement occurring as cooling rate increases and particle diameter decreases. In turn, the measurement of d_{eq} allows a Hall-Petch relation to be plotted. This is used to validate the occurrence of grain refinement and was shown Fig. 13, where a positive Hall-Petch relation is obtain such that $\sigma_y = \sigma_0 + \kappa_H A^{-0.25}$; where σ_y is the yield strength of the material, σ_0 is the friction stress, κ_H is Hall-Petch coefficient and A is the measured area of the dendrites.

Finally, the microhardness of the rapidly cooled samples is probed and found to increase with cooling rate. Although this is a standard observation attributed to grain refinement, another contributing factor which may not be neglected is the suppression of FCC growth. As the FCC is the softer phase in the alloy, its early suppression means that the hardness of the alloy is enhanced. However, it is also clear from Fig. 15 that between some powder sizes the microhardness remains relatively constant. This is explained by the idea

that the refinement of the ordered precipitates within the dendrites is expected to have an adverse effect on microhardness, leading to an apparent stagnation in certain regions of the plot. This non-conventional effect was first highlighted in Ni-based alloys containing significant volume fractions of ordered, Ni_3Al precipitates [33]. Namely, for dislocations to travel through the precipitates they must do so in pairs, as the first dislocation must first overcome the energy barrier to create an anti-phase boundary (APB). The second dislocation follows, removing the APB created by the leading dislocation. As such, the APB energy barrier is reduced as the precipitates in the AlCrCuFeNi dendrites decrease in size. This effect may be used to explain the stagnant regions in Fig. 15, where the strengthening due to grain refinement is being counterbalanced. Although this may explain the stagnant regions in Fig. 15, the overall increase in microhardness may be attributed to more than just grain boundary strengthening. Precipitation strengthening and dislocation strengthening are also known mechanisms that would result in increased microhardness [34,35]. Although potential contributions from dislocation strengthening have not been probed here as this is not pertinent to our atomised powders, precipitation strengthening is evident as d_{eq}, the equivalent diameter of the dendrites, decreases. With the decrease in d_{eq}, the density of the precipitates formed via SD within the dendrites visibly increases. Finally, the stark jumps in microhardness are attributed to developments in morphology whereby the first jump is attributed to increasingly fragmented dendrites. The second and final jump is attributed to the transition towards a simple solid solution structure, which in HEAs can lead to significant resistance to dislocation motion.

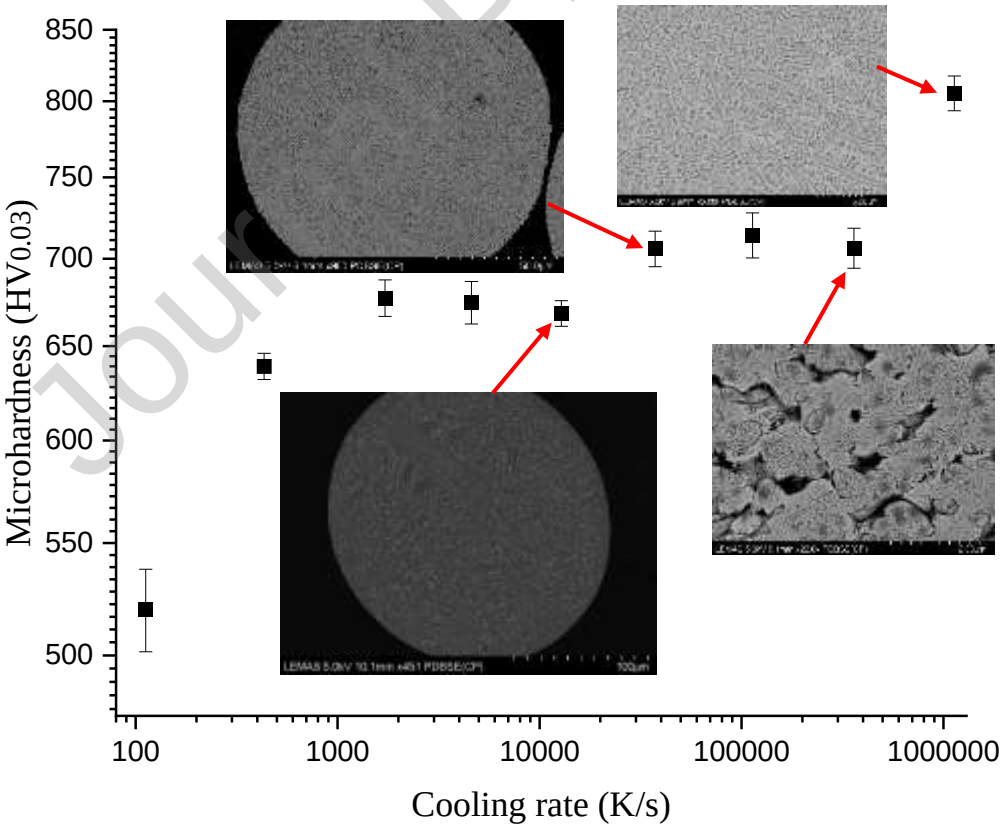

Fig. 15. Microhardness of AlCrCuFeNi powders as a function of average cooling rate.

5. Conclusions

In the present study, the rapid cooling of AlCrCuFeNi was achieved via containerless technique, resulting in powders with cooling rates ranging from 112 K/s to 1.13×10^6 K/s. The microstructures and properties of selected powder sizes are analysed, leading to the following conclusions:

1. The structure of as-cast AlCrCuFeNi was found to comprise four main components: a dendritic region, precipitates within the dendrites, a needle-like intermetallic (IM) seen along the periphery of the dendrites and deeper within the ID region, and finally, an inter-dendritic (ID) matrix.
2. An average cooling rate of 112 K/s is sufficient to inhibit FCC growth in equimolar AlCrCuFeNi HEA, leading to a single B2 solution.
3. Rapid solidification processing can successfully achieve AlCrCuFeNi HEAs with simple microstructures despite their apparently complex structures in the as-cast state.
4. The growth of the Cr and Fe rich, need-like phase observed in ID region of as-cast AlCrCuFeNi is inhibited at a cooling rate of around 1.13×10^6 K/s, leading to a simple solid solution structure.
5. Solid-state spinodally decomposed precipitates are observed in the dendrites of the as-cast AlCrCuFeNi HEA and AlCrCuFeNi powders. The formation of these precipitates is also inhibited only at the highest attained cooling rate of 1.13×10^6 K/s.
6. The microhardness of the powder droplets is found to increase with cooling rate from 519 $HV_{0.03}$ in the slowest cooled powder to 805 $HV_{0.03}$ in the fastest cooled powder.

Data Availability

Data will be made available upon request

References

[1] D.B. Miracle, J.D. Miller, O.N. Senkov, C. Woodward, M.D. Uchic, J. Tiley, Exploration and development of high entropy alloys for structural applications, Entropy. 16 (2014) 494–525. https://doi.org/10.3390/e16010494.

[2] Y. Zhang, T.T. Zuo, Z. Tang, M.C. Gao, K.A. Dahmen, P.K. Liaw, Z.P. Lu, Microstructures and properties of high-entropy alloys, Prog. Mater. Sci. 61 (2014) 1–93. https://doi.org/10.1016/j.pmatsci.2013.10.001.

[3] D.B. Miracle, O.N. Senkov, A critical review of high entropy alloys and related concepts, Acta Mater. 122 (2017) 448–511. https://doi.org/10.1016/j.actamat.2016.08.081.

[4] Z. Li, K.G. Pradeep, Y. Deng, D. Raabe, C.C. Tasan, Metastable high-entropy dual-phase alloys overcome the strength-ductility trade-off, Nature. 534 (2016) 227–230. https://doi.org/10.1038/nature17981.

[5] B.S. Murty, S. Ranganathan, J.W. Yeh, P.P. Bhattacharjee, High-entropy alloys, 2019. https://doi.org/10.1016/C2017-0-03317-7.

[6] Z. Li, C.C. Tasan, K.G. Pradeep, D. Raabe, A TRIP-assisted dual-phase high-entropy alloy: Grain size and phase fraction effects on deformation behavior, Acta Mater. 131 (2017) 323–335. https://doi.org/10.1016/j.actamat.2017.03.069.

[7] Q. Guo, X. Xu, X. Pei, Z. Duan, P.K. Liaw, H. Hou, Y. Zhao, Predict the phase formation of high-entropy alloys by compositions, J. Mater. Res. Technol. 22 (2023) 3331–3339. https://doi.org/10.1016/j.jmrt.2022.12.143.

[8] M.H. Tsai, J.W. Yeh, High-entropy alloys: A critical review, Mater. Res. Lett. 2 (2014) 107–123. https://doi.org/10.1080/21663831.2014.912690.

[9] H.W. Luan, Y. Shao, J.F. Li, W.L. Mao, Z.D. Han, C. Shao, K.F. Yao, Phase stabilities of high entropy alloys, Scr. Mater. 179 (2020) 40–44. https://doi.org/10.1016/j.scriptamat.2019.12.041.

[10] F. Otto, Y. Yang, H. Bei, E.P. George, Relative effects of enthalpy and entropy on the phase stability of equiatomic high-entropy alloys, Acta Mater. 61 (2013) 2628–2638. https://doi.org/10.1016/j.actamat.2013.01.042.

[11] Y. Guo, H. Su, H. Zhou, Z. Shen, Y. Liu, J. Zhang, L. Liu, H. Fu, Unique strength-ductility balance of AlCoCrFeNi2.1 eutectic high entropy alloy with ultra-fine duplex microstructure prepared by selective laser melting, J. Mater. Sci. Technol. 111 (2022) 298–306. https://doi.org/10.1016/j.jmst.2021.10.013.

[12] H. Jiang, K. Han, X. Gao, Y. Lu, Z. Cao, M.C. Gao, J.A. Hawk, T. Li, A new strategy to design eutectic high-entropy alloys using simple mixture method, Mater. Des. 142 (2018) 101–105. https://doi.org/10.1016/j.matdes.2018.01.025.

[13] S. Luo, P. Gao, H. Yu, J. Yang, Z. Wang, X. Zeng, Selective laser melting of an equiatomic AlCrCuFeNi high-entropy alloy: Processability, non-equilibrium microstructure and mechanical behavior, J. Alloys Compd. 771 (2019) 387–397. https://doi.org/10.1016/j.jallcom.2018.08.290.

[14] P. Jinhong, P. Ye, Z. Hui, Z. Lu, Microstructure and properties of AlCrFeCuNi x ($0.6 \leq x \leq 1.4$) high-entropy alloys, Mater. Sci. Eng. A. 534 (2012) 228–233. https://doi.org/10.1016/j.msea.2011.11.063.

[15] C. Zhang, J. Zhu, H. Zheng, H. Li, S. Liu, G.J. Cheng, A review on microstructures and properties

of high entropy alloys manufactured by selective laser melting, Int. J. Extrem. Manuf. 2 (2020). https://doi.org/10.1088/2631-7990/ab9ead.

[16] X. Wang, W. Guo, Y. Fu, High-entropy alloys: Emerging materials for advanced functional applications, J. Mater. Chem. A. 9 (2021) 663–701. https://doi.org/10.1039/d0ta09601f.

[17] X. Wang, Y. Zhang, X. Ma, High temperature deformation and dynamic recrystallization behavior of AlCrCuFeNi high entropy alloy, Mater. Sci. Eng. A. 778 (2020). https://doi.org/10.1016/j.msea.2020.139077.

[18] V. Shivam, S. Kar, G.K. Mandal, V.C. Srivastava, Microstructural evolution and phase selection during solidification of AlCrCuFeNi high entropy alloy, J. Alloys Compd. (2023). https://doi.org/10.1016/j.jallcom.2023.171261.

[19] A.E. Nassar, A.M. Mullis, Rapid screening of high-entropy alloys using neural networks and constituent elements, Comput. Mater. Sci. 199 (2021) 110755. https://doi.org/10.1016/j.commatsci.2021.110755.

[20] L. Cao, P. Hou, A. Nassar, A.M. Mullis, Dendritic growth of rapid-solidified eutectic high-entropy alloy, in: Mater. Sci. Forum, 2021: pp. 46–50. https://doi.org/10.4028/www.scientific.net/MSF.1035.46.

[21] M.R. Abul, R.F. Cochrane, A.M. Mullis, A. Nassar, Microstructural Evolution and Mechanical Properties of Drop Tube Processed Al-4.1 wt.% Fe-1.9 wt.% Si, J. Mater. Eng. Perform. (2023). https://doi.org/10.1007/s11665-023-08561-6.

[22] O. Oloyede, T.D. Bigg, R.F. Cochrane, A.M. Mullis, Microstructure evolution and mechanical properties of drop-tube processed, rapidly solidified grey cast iron, Mater. Sci. Eng. A. 654 (2016) 143–150. https://doi.org/10.1016/j.msea.2015.12.020.

[23] F. Cardarelli, Materials Handbook — a concise desktop reference, Mater. Des. 22 (2001) 237. https://doi.org/10.1016/s0261-3069(00)00075-3.

[24] J.H. Awbery, E. Griffiths, The latent heat of fusion of some metals, Proc. Phys. Soc. London. 38 (1925) 378–398. https://doi.org/10.1088/1478-7814/38/1/343.

[25] E.S. Lee, S. Ahn, Solidification progress and heat transfer analysis of gas-atomized alloy droplets during spray forming, Acta Metall. Mater. 42 (1994) 3231–3243. https://doi.org/10.1016/0956-7151(94)90421-9.

[26] Y.Z. Li, Y. Shi, Microstructure and process optimization of AlCrFeCoNiCu high-entropy alloy by laser deposition, Guangxue Jingmi Gongcheng/Optics Precis. Eng. 27 (2019) 795–806. https://doi.org/10.3788/OPE.20192704.0795.

[27] S. Guo, C. Ng, C.T. Liu, Anomalous solidification microstructures in Co-free Al xCrCuFeNi2 high-entropy alloys, J. Alloys Compd. 557 (2013) 77–81. https://doi.org/10.1016/j.jallcom.2013.01.007.

[28] C.J. Tong, Y.L. Chen, S.K. Chen, J.W. Yeh, T.T. Shun, C.H. Tsau, S.J. Lin, S.Y. Chang, Microstructure characterization of AlxCoCrCuFeNi high-entropy alloy system with multiprincipal elements, Metall. Mater. Trans. A Phys. Metall. Mater. Sci. 36 (2005) 881–893. https://doi.org/10.1007/s11661-005-0283-0.

[29] S. Singh, N. Wanderka, B.S. Murty, U. Glatzel, J. Banhart, Decomposition in multi-component AlCoCrCuFeNi high-entropy alloy, Acta Mater. 59 (2011) 182–190. https://doi.org/10.1016/j.actamat.2010.09.023.

[30] Y. Zhang, Z. Chen, D. Cao, J. Zhang, P. Zhang, Q. Tao, X. Yang, Concurrence of spinodal decomposition and nano-phase precipitation in a multi-component AlCoCrCuFeNi high-entropy alloy, J. Mater. Res. Technol. 8 (2019) 726–736. https://doi.org/10.1016/j.jmrt.2018.04.020.

[31] R. Wang, K. Zhang, C. Davies, X. Wu, Evolution of microstructure, mechanical and corrosion properties of AlCoCrFeNi high-entropy alloy prepared by direct laser fabrication, J. Alloys Compd. 694 (2017) 971–981. https://doi.org/10.1016/j.jallcom.2016.10.138.

[32] Y. Wang, R. Li, P. Niu, Z. Zhang, T. Yuan, J. Yuan, K. Li, Microstructures and properties of equimolar AlCoCrCuFeNi high-entropy alloy additively manufactured by selective laser melting, Intermetallics. 120 (2020). https://doi.org/10.1016/j.intermet.2020.106746.

[33] A. Vattré, B. Devincre, A. Roos, Dislocation dynamics simulations of precipitation hardening in Ni-based superalloys with high γ′ volume fraction, Intermetallics. 17 (2009) 988–994. https://doi.org/10.1016/j.intermet.2009.04.007.

[34] X. Liu, K. Song, Z. Kou, J. Gong, X. Chen, Q. Gao, H. Sun, P. Liu, R. Qu, L. Hu, Z. Zhang, P. Ramasamy, Z. Liu, Z. Zhang, F. Liu, Z. Zhang, J. Eckert, Synergistic grain boundary engineering for achieving strength-ductility balance in ultrafine-grained high-Cr-bearing multicomponent alloys, Int. J. Plast. 177 (2024). https://doi.org/10.1016/j.ijplas.2024.103992.

[35] S. Liu, T. Sun, Z. Kou, X. Han, Q. Gao, J. Zhang, X. Liu, L.C. Zhang, J. Orava, K. Song, L. Xiao, J. Eckert, W. Song, Promising pathways for balancing strength and ductility in chemically complex alloys with medium-to-high stacking fault energies, Int. J. Plast. 190 (2025). https://doi.org/10.1016/j.ijplas.2025.104358.

Declaration of interests

☒ The authors declare that they have no known competing financial interests or personal relationships that could have appeared to influence the work reported in this paper.

☐ The author is an Editorial Board Member/Editor-in-Chief/Associate Editor/Guest Editor for *[Journal name]* and was not involved in the editorial review or the decision to publish this article.

☐ The authors declare the following financial interests/personal relationships which may be considered as potential competing interests: